paleocurrents and intraformational unconformities in the rocks suggest that the integrated Chinle-Dockum depositional system was disrupted when rift-related structures began to form (*29*).

REFERENCES AND NOTES

1. T. F. Lawton, in *Mesozoic Systems of the Rocky Mountain Region, USA*, M. V. Caputo, J. A. Peterson, K. J. Franczyk, Eds. (Society for Sedimentary Geology, Denver, CO, 1994), pp. 1–35.
2. For example, P. L. Abbott and T. E. Smith, *Geology* **17**, 329 (1989).
3. J. H. Stewart, *U.S. Geol. Surv. Prof. Pap. 690* (1972); ———, T. H. Anderson, G. B. Haxel, L.T. Silver, J. E. Wright, *Geology* **14**, 567 (1986).
4. S. G. Lucas, *N.M. Bur. Mines Min. Resour. Bull.* **137**, 47 (1991).
5. G. E. Gehrels and W. R. Dickinson, *Am. J. Sci.* **295**, 18 (1995).
6. T. M. Lehman, *N.M. Bur. Mines Min. Resour. Bull.* **34**, 37 (1994); *West Tex. Geol. Soc. Bull.* **34**, 5 (1994).
7. S. G. Lucas and A. P. Hunt, *J. Ariz. Nev. Acad. Sci.* **22**, 21 (1987).
8. Mean $Q_{93}F_2L_5$, n = 78 (*10*); J. Schnable, thesis, Texas Tech University (1994).
9. J. Schnable, unpublished data.
10. T. Fritz, thesis, Texas Tech University (1991).
11. Paleoflow direction 113, n = 408 [B. May, thesis, Texas Tech University (1988); (*8–10*)].
12. R. E. Dunay and M. J. Fisher, *Rev. Palaeobot. Palynol.* **28**, 61 (1979).
13. W. B. Harland *et al.*, *A Geologic Time Scale 1989* (Cambridge Univ. Press, Cambridge, 1990).
14. R. F. Dubiel, in (*1*), pp. 133–168.
15. Approximately 30 kg of the Santa Rosa Sandstone were collected from a cut bank along Sierrita de la Cruz Creek in Potter County, Texas [locality SDC1 of (*9*)]. The sandstone here unconformably overlies the Quartermaster Formation, a succession of Permian red beds. The sample was crushed, and zircons were separated by standard methods. The zircon separate was sieved to >100 μm, and the largest zircons, generally 125 to 150 μm in longest dimension, were picked into six fractions on the basis of color, shape, and lack of inclusions. Grains were abraded for ~4 hours and analyzed individually. Dissolution in 0.1-ml microcapsules within a 125-ml digestion chamber was followed by recycling with a mixed ^{205}Pb-^{235}U spike and standard chemical separation of Pb and U. The elements were loaded with silica gel onto Re filaments and analyzed with a VG-354 mass spectrometer in static mode with the use of three Faraday collectors and a Daly detector system for Pb and two Faraday collectors for UO_2. The time scale of Harland *et al.* (*13*) is used to correlate isotopic and faunal ages.
16. M. A. Fracasso and A. Kolker, *West Tex. Geol. Soc. Bull.* **24**, 5 (1985).
17. M. Ruiz-Castellanos, thesis, University of Texas (1976); A. J. Jacobo, *Rev. Inst. Mex. Pet.* **18**, 5 (1986); V. R. Torres, J. Ruiz, M. Grajales, G. Murillo, *Geol. Soc. Am. Abstr. Prog.* **24**, A64 (1992).
18. R. Slingerland and K. P. Furlong, *Geomorphology* **2**, 23 (1989).
19. L. E. Long and T. Lehman, *U.S. Geol. Surv. Circ.* **1107**, 197 (1994).
20. R. E. Denison, G. S. Kenny, W. H. Burke Jr., E. A. Hetherington Jr., *Geol. Soc. Am. Bull.* **80**, 245 (1969); J. D. Gleason, P. J. Patchett, W. R. Dickinson, J. Ruiz, *ibid.* **107**, 1192 (1995).
21. Probable age of 525 ± 25 Ma based on feldspar, biotite, and whole-rock Rb-Sr and zircon U-Pb [W. E. Ham, R. E. Denison, C. A. Merritt, *Okla. Geol. Surv. Bull. 95* (1964)].
22. P. Hoffman, *Annu. Rev. Earth Planet. Sci.* **16**, 543 (1988).
23. J. H. Stewart, *Nev. Bur. Mines Geol. Spec. Publ. 4* (1980), p. 136; E. A. Johnson *et al.*, *Geol. Soc. Am. Abstr. Prog.* **25**, 57 (1993); S. G. Lucas and T. H. Goodspeed, *ibid.*, p. 111.
24. R. Lupe and N. J. Silberling, in *Tectonostratigraphic Terranes of the Circum-Pacific Region*, D. G. Howell, Ed. (Circum-Pacific Council for Energy and Mineral Research, Houston, TX, 1985), pp. 263–271; M. W. Elison and R. C. Speed, *Geol. Soc. Am. Bull.* **100**, 185 (1988).
25. n = 3 in Osobb, compared with n = 1 in Santa Rosa Sandstone.
26. U. Schärer and C. J. Allegre, *Nature* **295**, 585 (1982); O. Tweto, *U.S. Geol. Surv. Prof. Pap. 1321-A* (1987), p. 54.
27. M. E. Bickford, R. L. Cullers, R. D. Shuster, W. R. Premo, W. R. Van Schmus, *Geol. Soc. Am. Spec. Pap. 235* (1989), p. 33; M. E. Bickford, R. D. Shuster, S. J. Boardman, *ibid.*, p. 49.
28. Compare W. R. Dickinson, in *Relations of Tectonics to Ore Deposits in the Southern Cordillera*, W. R. Dickinson and W. D. Payne, Eds. (Arizona Geological Society Digest , 1981), vol. 14, pp. 113–135.
29. T. Lehman, unpublished data.
30. K. R. Ludwig, *U.S. Geol. Surv. Open-File Rep. 88-542* (1991)
31. J. S. Stacey and J. D. Kramers, *Earth Planet. Sci. Lett.* **26**, 207, (1975).

32. Acknowledgment by N.R.R. is made to the Donors of The Petroleum Research Fund, administered by the American Chemical Society, for support of this research. Support for zircon geochemistry and analysis was provided by National Science Foundation grant EAR-9416933 (G.E.G.). We thank R. F. Dubiel, J. D. Gleason, T. F. Lawton, S. G. Lucas, F. J. Pazzaglia, and R. Slingerland for discussions; T. F. Lawton for review of an earlier version of the manuscript; and J. Ruiz for information about Permian plutons in Mexico. We thank J. P. Schnable for sample collection and A. L. Roach for zircon separation.

6 February 1996; accepted 3 May 1996

Late Proterozoic and Paleozoic Tides, Retreat of the Moon, and Rotation of the Earth

C. P. Sonett,* E. P. Kvale, A. Zakharian, Marjorie A. Chan, T. M. Demko

The tidal rhythmites in the Proterozoic Big Cottonwood Formation (Utah, United States), the Neoproterozoic Elatina Formation of the Flinders Range (southern Australia), and the Lower Pennsylvanian Pottsville Formation (Alabama, United States) and Mansfield Formation (Indiana, United States) indicate that the rate of retreat of the lunar orbit is $d\xi/dt \sim k_2 \sin(2\delta)$ (where ξ is the Earth-moon radius vector, k_2 is the tidal Love number, and δ is the tidal lag angle) and that this rate has been approximately constant since the late Precambrian. When the contribution to tidal friction from the sun is taken into account, these data imply that the length of the terrestrial day 900 million years ago was ~18 hours.

The well-known tides induced on Earth by the sun and moon have had several long-term effects over the age of Earth. Most notably, the transfer of angular momentum from Earth to the moon has resulted in an appreciable increase in the length of the day and a retreat of the moon from Earth. Here, we used laminated tidal sediments to determine tidal periods back to 900 million years ago. From these records, the retreat rate of the moon—that is, the evolution in time of the lunar semimajor axis—can be calculated. In principle, the information derived from tidal rhythmites (tidalites) can also yield the rotational deceleration of Earth, the change in the length of day (LOD), the rate of generation of terrestrial tidal frictional heat, and the variation with time of the product of k_2 and $\sin(2\delta)$. Tidalites consist of stacked sets (commonly of millimeter to centimeter scale) of laminated mudstone or intercalated beds of sandstone and mudstone; successive sets exhibit progressive vertical thickening and thinning in response to daily changes in current velocities associated with tidal processes. Tidalites from a variety of modern settings—including delta fronts, abandoned tidal channels, tidal flats, and estuaries—have been described (*1*).

The most common reported tidal cyclicities in the rock record include daily, semidaily, and semimonthly periods. Semimonthly (neap-spring) periods reflect phase changes of the moon during the half-synodic month and lunar declinational changes associated with the half-tropical month (*2*). During the synodic month, tides are higher when Earth, the moon, and the sun are nearly aligned (syzygy) and are lower when the radius vectors from Earth to the sun and moon enclose a right angle (quadrature). Spring tides form during syzygy (full and new moon), whereas neap tides form during quadrature (the waxing and waning phases of the moon) (*3*). Deviations from tidal equilibrium are always encountered in the tidal record (*4*); these deviations result from local tidal geometry and variable basinal

C. P. Sonett, Department of Planetary Sciences and Lunar and Planetary Laboratory, University of Arizona, Tucson, AZ 85721, USA.
E. P. Kvale, Indiana Geological Survey, Indiana University, Bloomington, IN 47405, USA.
A. Zakharian, Lunar and Planetary Laboratory, University of Arizona, Tucson, AZ 85721, USA.
M. A. Chan, Department of Geology and Geophysics, University of Utah, Salt Lake City, UT 84112, USA.
T. M. Demko, Department of Earth Resources, Colorado State University, Fort Collins, CO 80523, USA.

*To whom correspondence should be addressed.

harmonic response. Ideally, the lunar synodic period is estimated by determining the neap-spring events in a solar year; this approach avoids counting errors arising from possible losses of individual laminae. Effects of ancient basinal harmonics are often difficult to subtract from the rock record. Such corrupting effects can be avoided by restricting analysis to the neap-spring cycle or by using very long records of the individual semidaily events. We primarily examined laminae group widths corresponding to neap-spring cycles associated with the half-synodic month.

The tidal sequences we analyzed are preserved in the Big Cottonwood Formation (BCC) in Utah, 900 ± 100 Ma (million years ago) (Fig. 1) (*5*); the Elatina Formation of southern Australia, 650 ± 100 Ma (*6*); the Pottsville Formation of northern Alabama, 312 ± 5 Ma (*7*); and the Hindostan whetstone beds in the Mansfield Formation of Indiana, 305 ± 5 Ma (*8*). These records are separated in time by intervals of ~300 million years (My). The Mansfield and Pottsville tidalite ages are based on biostratigraphic and lithostratigraphic correlations; the ages of the Elatina Formation and BCC are estimated from adjoining igneous rocks. The thickness of the tidalites in each formation is variable but is generally a few millimeters. After the cores were halved and polished to optimize contrast, we counted the tidalites with the use of a binocular microscope fitted with a micrometer.

Neap-spring counting previously reported for the Elatina Formation has yielded a mean rate of lunar retreat from the late Precambrian to the present (*6*). The lunar orbital period has also been inferred from studies of intertidal Devonian corals and other biota (*9*). These studies suggested that the length of the year was ~400 days at 345 to 395 Ma; this estimate implies a geologically late close approach of the moon to Earth, but there is no evidence of the "megatides" and extraordinary heating that would have resulted (*10, 11*).

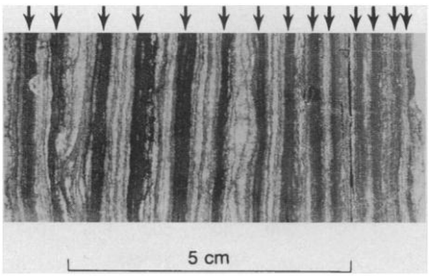

Fig. 1. Photograph of polished core of BCC tidalites. Laminae of coarse silt to fine-grained sand were transported only during the strongest spring tides. The thick dark bands (arrows) correspond to neap-tide deposition of fine-grained mud.

Both the moon and sun induce gravitational quadrupole moments in Earth. The tidal bulge "leads" the Earth-moon and Earth-sun radius vectors by tidal lag angles. Tides raised by the moon are some five times those raised by the sun; the two tidal perturbations approximately converge at syzygy. Angular momentum from Earth's spin couples to both the lunar orbit and (to a lesser extent) Earth's orbit about the sun. The transfer of angular momentum to the moon's orbit leads to an increase of the major axis of the moon's orbit at the expense of Earth's rotation rate. The lunar and solar gravitational potentials, respectively, at an arbitrary point P on Earth's surface are

$$\phi_m = -GM_m \frac{1+\left[\frac{M_m}{2(M_e + M_m)}\right]}{\xi} - GM_m a^2 \frac{\left(\frac{3\cos^2\psi_m}{2} - \frac{1}{2}\right)}{\xi^3} - \frac{(\omega_L a \sin\omega_m)^2}{2} \quad (1)$$

$$\phi_s = -GM_e \frac{1+\left[\frac{M_e}{2(M_s + M_e)}\right]}{\xi} - GM_e a^2 \frac{\left(\frac{3\cos^2\Psi_s}{2} - \frac{1}{2}\right)}{\xi^3} - \frac{(\omega_L a \sin\omega_s)^2}{2} \quad (2)$$

(*12*), where the subscripts m, s, and e refer to the moon, sun, and Earth, respectively; M is mass; ω_L is orbital angular velocity (about the center of mass of the system); Ψ is the direction angle to P measured from the moon or sun; ξ is the radius vector; $\cos\Psi = \sin\theta\cos\lambda$ (where θ is the colatitude of P, $\lambda = \omega t$ is the time-dependent longitude measured eastward from the radius vector, ω is rotational angular velocity, and t is time); a is the radius of Earth; and G is the universal constant of gravitation (*13*). In both equations, the second term on the right defines the tidal deformation, and the third term is the centrifugal potential at P resulting from the rotation of Earth about the common center of mass of the system (Earth-moon in Eq. 1 and Earth-sun in Eq. 2). The tide raised on Earth by the moon and the sun, respectively, can be written as

$$\phi'_m = -GM_m a^2 \frac{3\cos^2\psi_m - 1}{2\xi_m^3} \quad (3)$$

$$\phi'_s = -GM_s a^2 \frac{3\cos^2\psi_s - 1}{2\xi_s^3} \quad (4)$$

The total terrestrial disturbance potential caused by the moon and sun is

$$\phi'_{tot} = \phi'_m + \phi'_s \quad (5)$$

where ϕ'_m and ϕ'_s are the lunar and solar disturbance potentials, respectively. The equilibrium tide corresponding to ϕ_m is raised semidiurnally on a rotating Earth where the spin axis is normal to the plane of the moon's orbit. For the present-epoch Earth, with orbital obliquity of 23.5° ± 1.5°, the so-called tidal inequality introduces a strong latitude-dependent inequality (which vanishes on the equator) in the two semidiurnal tides. The combination of lunar and solar tidal contributions considerably alters the tidal problem because of the diurnal inequality of the tides, which are generally not collinear.

Our major specific aim in the data analysis was to determine the number of neap-spring cycles per year. The year (the orbital period of Earth) is reasonably assumed to be invariant since the Precambrian. In that case, if a yearly (seasonal) period can be found, the power spectral density of the time sequence of neap-spring periods re-

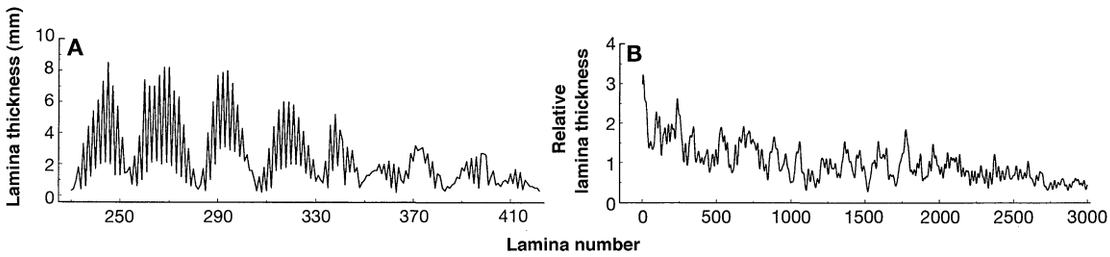

Fig. 2. (**A**) Time sequence record of selected part of the Mansfield laminae sequence, showing several neap-spring cycles. A strong diurnal inequality is disclosed, indicating a mid-latitude origin. (**B**) Corresponding full Pottsville record of 3000 laminae.

veals the synodic neap-spring frequency f_n. The corresponding sidereal period is $\tau_{sid} = 2/f_n - 1$; the factor of 2 corresponds to the two neap-spring periods per lunar orbital period. The semimajor axis is given by

$$\xi = \left(\frac{\tau_{sid}}{2\pi}\right)^{2/3} [G(M_m + M_e)]^{1/3} \qquad (6)$$

where eccentricity is ignored.

To capture the neap-spring cyclicity in the BCC records, we reconstructed the core time sequence with a singular spectrum analysis (SSA) algorithm (*14*) followed by computation of the periodogram [discrete Fourier transform (DFT)]. We checked the results by direct counting of neap-spring interval thicknesses. Because SSA removes much of the noise component by eigenvalue selection for the reconstruction, the 2σ error bounds were also determined by maximum likelihood estimation (MLE) and the raw time sequence with initial frequency guesses from the DFT (*15*); statistical error bounds from MLE using raw data sequences contain the complete spectrum of noise as well as data and are the most meaningful measure of noise error (*16*). The BCC data yielded a semimajor axis of 3.45×10^{10} cm. Corrections for apsidal rotation of the moon's orbit and nodal regression are ignored because these corrections are of the same order as the computed random errors of the data.

Previous reports on the Elatina data (*6*) used the neap-spring (dark band) data. The calculation we report is based on MLE; our retreat rate is somewhat higher and is more consistent with the Apollo data (data gathered by means of the laser reflector deposited on the moon during the Apollo program) and the BCC data. The Elatina tidalites appear to be the most noise-free records available; MLE confirms that the noise is low.

The Pennsylvanian records (Mansfield and Pottsville) (Fig. 2) are more difficult to decode because the primary data are individual laminae and any yearly signal is of insufficient clarity to provide a yearly neap-spring count. Moreover, without an absolute (for example, annual) time reference, these data correspond only to the number of terrestrial rotations per lunar orbital period; hence, the periods are lower bounds of the true lunar orbital period. The Mansfield periodogram (Fig. 3A) discloses a cluster of four lines, ranging in synodic frequency from 0.035 to 0.045 per lamina, which yield a spread of semimajor axis values. If the record of individual laminae is subject to erosion and loss of laminae, the least affected frequency (based on a scaled spectrum) is the lowest frequency. For the Mansfield Formation, this synodic frequency is 0.035 per lamina, which is the value used in the computation of the orbital curve of growth (OCG). Attempts to "tune" the spectrum to basic semiannual and annual tidal periods are not sufficiently viable; further work may yield an improved Pennsylvanian estimate of the lunar orbital period.

To improve the signal/noise ratio of the Pottsville record, we reconstructed the time sequence with SSA (maximum autocovariance lag = 400; eigenvalue spectrum rank from 1 to 12). Fig. 3B gives the DFT of the subsequent computation of the spectrum from the reconstruction. The long-period record consists of a remarkable sequence of relatively narrow lines, of which the two longest periods suggest annual and semiannual lines with ~5 to 10% loss of laminae. As in the case of the Mansfield data, attempts to tune the frequency scale of the spectrum have not yet been successful, and we use the same argument to select the spectral line at 0.035 per lamina as the least corrupted.

The linear least squares (LLS) "floating" fit (that is, a fit unconstrained by the Apollo data–derived retreat rate) uses BCC, Elatina, and Mansfield period estimates (Fig. 4). The least squares (LS) fit gives a mean retreat rate of 3.25 cm year^{-1}; it is influenced somewhat by the small error for the Mansfield data and more strongly by the small range estimate for age. For completeness, Fig. 4 also shows a linear extrapolation from the present retreat rate and semimajor axis of the moon's orbit. It passes through

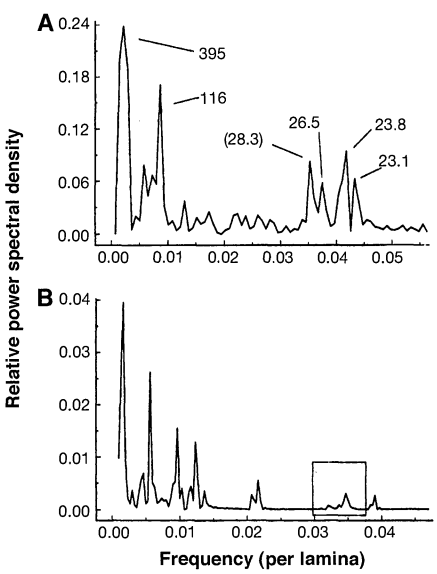

Fig. 3. (**A**) Periodogram of the Mansfield synodic data, showing a neap-spring region cluster. The lunar orbital period corresponding to each peak (in days) is shown; the value of 28.3 (in parentheses) is the only member consistent with the Pottsville data. (**B**) DFT of SSA reconstruction of the Pottsville data. The boxed area is the neighborhood of the expected neap-spring period. Other peaks can be identified (with periods ranging downward from annual) but appear to be corrupted by loss of laminae. Only the line at 0.035 per lamina provides a period consistent with the neap-spring period.

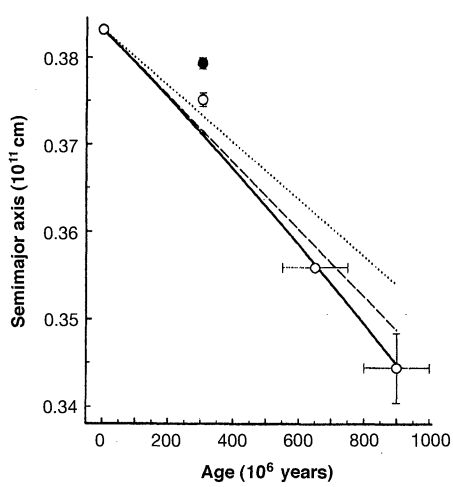

Fig. 4. OCG derived from lunar orbital period estimates from tidalite measurements. The modern value and estimates from Mansfield data (305 Ma, ○), Pottsville data (312 Ma, ●), Elatina data (650 Ma), and BCC data (900 Ma) are shown. Error bars for Elatina and BCC (±100 My) are not relevant to estimates of the lunar orbital period; these bars are absent for the Pottsville and Mansfield data because of the small age uncertainty (± ~5 My). The dashed line is a constant-slope datum using Apollo values for ξ and $d\xi/dt$ = 3.82 cm year^{-1}. The dotted line is a LLS fit to the four data, unconstrained by the Apollo $d\xi/dt$. The solid line is a second-order LS fit constrained by the Apollo $d\xi/dt$.

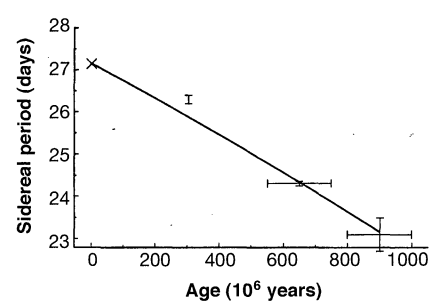

Fig. 5. Sidereal lunar orbital period (in present-epoch days) versus age. The 300-My value (Mansfield and Pottsville data) should be revised upward by a small but uncertain increment subject to an unknown absolute time reference.

Table 1. Tidalite-derived synodic lunar orbital periods.

Formation	Period (days)	$+2\sigma$	-2σ
BCC	25.0	25.3	24.7
Elatina	26.2	26.2	26.2
Pottsville	28.7	28.8	28.3
Mansfield	28.3	28.2	28.4
Modern	29.5	—	—

the Elatina-derived value of ξ and just grazes the 2σ error estimate from the BCC data.

Calculation of the second-order LS OCG (Fig. 4) is constrained by the Apollo data–derived retreat rate, $d\xi/dt = 3.82 \pm 0.07$ cm year^{-1} (*17*), and more generally by the requirement that $d\xi/dt \leq 0$ so long as angular momentum flows from Earth (or, equivalently, that ϕ_{tot} corresponds to a tidally "leading" Earth). The value for ξ is given for the present epoch (*18*). The response of the sun to the solar tide raised on Earth is to feed angular momentum from the sun into Earth's orbit. The sun's contribution to the Earth-moon problem can be handled as a perturbation to Earth's rotation and is therefore not included directly in the following discussion. However, the sun's tidal potential affects Earth markedly through friction and the LOD.

The Pottsville and Mansfield data (Fig. 4) lie $\sim 5\sigma$ to 6σ away from the regression lines. For the Pottsville, Mansfield, and Elatina data, the errors in age are too small to show as error bars. The Pottsville and Mansfield data may genuinely lie this far from the computed regression line; alternatively, they may be affected by a bias to smaller ξ (from laminae erosion), a bias to larger ξ (because of the lack of an absolute time base), or both. We have included these data because of the potential importance of the displacement from the OCG-computed variation of ξ with time. The errors shown in Fig. 4 and discussed here are assumed normally distributed random. The possibility of significant (nonrandom) error from biases remains possible for the Pennsylvanian data.

Because the second-order LS fit (Fig. 4) is not strictly linear, the working hypothesis is that nonconstant tidal friction from the late Proterozoic to the present cannot be ruled out and requires a longer record of tides. Such a nonlinearity is consistent with the breakup of Pangaea and the development of shallow seas and higher friction in the Paleozoic. However, wave drag and the potential importance of oceanic resonances leave this matter unresolved (*19*). The sidereal lunar orbital periods for the BCC, Elatina, Mansfield, and modern geological times are shown in Fig. 5 (with 2σ error estimates and associated estimates of age uncertainties) and are listed in Table 1. If we assume that eccentricity can be ignored, the torque T on the moon's orbit (ignoring the sun's contribution) is obtained by differentiating Eq. 3 with respect to Ψ,

$$T = \frac{3}{2}\left[\frac{G(M_m^2\, a^5)}{\xi^6}\right] k_2 \sin(2\delta) \qquad (7)$$

so that for constant $\dot{\xi}$ (that is, constant $d\xi/dt$),

$$\xi^{11/2} \sim k_2 \sin(2\delta) \qquad (8)$$

which implies a powerful increase in $k_2 \sin(2\delta)$ with increasing ξ. Solving Eqs. 7 and 8 for δ yields

$$\delta \sim 0.43\frac{\dot{\xi}}{k_2} \qquad (9)$$

for small values of δ, where $\dot{\xi}$ is in centimeters per year and δ is in degrees.

The lag angle is often assumed fixed. However, if Takeuchi's k_e [see (*19*)] is held fixed versus time, which seems reasonable, then the lag angle must evolve. Figure 6 gives the lunitidal angle for $0.31 \leq k_e \leq 0.356$ for the assumption of constant friction. The lag angle δ varies from 3.2° to 4.6° for the smallest value of k_e, and correspondingly for larger k_e. Corresponding quality factors Q range from ~11 to 19; this range is compatible with earlier derivations from Holocene data. Generally, δ varies by ~1.6° independently of the Love number.

Munk and MacDonald (*20*) estimated the present rotational deceleration of Earth attributable only to the lunar tidal component to be -4.81×10^{-22} rad s^{-2}. The BCC (900 Ma) tidalite data indicate that if only the lunar component is considered, the LOD was 19.2 hours during the late Proterozoic. If the solar component of 21% is added (assuming a common k_2 value), then the LOD was ~18.2 hours at that time (Table 2).

The energy of the lunar orbit with time increases (as the major axis grows) at the expense of Earth's rotational energy. The effect is to lengthen the monthly cycle observed in the sedimentary record. In all, $1.32 \pm 0.18 \times 10^{35}$ ergs of terrestrial rotational energy was lost over the past 900 My. The gain in orbital energy of the moon during this time was $3.40 \pm 0.03 \times 10^{35}$ ergs. The difference appears as thermal (frictional) energy, where the generated heat $H_{mean} = 2.92 \times 10^{19}$ erg s^{-1} (excluding any solar contribution) (*21*, *22*). This value is ~50% of that estimated by Munk and MacDonald, but it is a mean over 900 My during which time, based on the increase in tidal coupling with time, the frictional loss would have varied. This value is ~10% that of the present-day mantle radioactive heat production (8.5×10^{12} cal s^{-1} or 4.5×10^{-8} cal g^{-1} year^{-1}) (*22*). Table 2 gives a summary of parameters for BCC time (900 Ma).

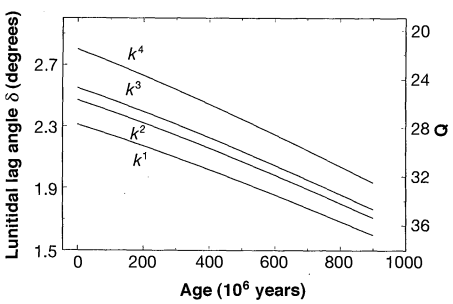

Fig. 6. Estimate of $k_2 \sin(2\delta)$ versus age and Q. Calculations are based on second-order LS fit to data (constrained by the Apollo $d\xi/dt$). In terms of Takeuchi's k_e (*20*), $k^1 = 0.256$ (density, 2.7 g cm^{-3}); $k^2 = 0.281$ (density, 3.0 g cm^{-3}) (*22*); $k^3 = 0.29$ (*23*); and $k^4 = 0.31$ (*22*).

Table 2. Late Proterozoic (900 Ma) lunitidal parameters for BCC data. Values in parentheses are incremented by 21% to include the solar contribution to tidal friction. The $+2\sigma$ error estimates are based only on internal Gaussian (normally distributed) noise.

Parameter	Mean	$+2\sigma$	-2σ
Sidereal period (days)	23.4	23.6	23.1
Semimajor axis (cm)	3.453×10^{10}	3.478×10^{10}	3.429×10^{10}
Orbital momentum (g cm^2 s^{-1})	2.727×10^{41}	2.737×10^{41}	2.717×10^{41}
Torque (dyne·cm)	9.600×10^{23}	9.636×10^{23}	9.567×10^{23}
Orbital energy (ergs)	-4.242×10^{35}	-4.212×10^{35}	-4.272×10^{35}
Length of day (hours)	19.2 (18.2)	19.0 (17.9)	19.5 (18.5)
Days per year	456 (481)	462 (489)	450 (473)

REFERENCES AND NOTES

1. H. R. Feldman *et al.*, *Palaios* **8**, 485 (1993).
2. A. W. Archer, E. P. Kvale, H. R. Johnson, in *Clastic Tidal Sedimentology*, D. G. Smith, G. E. Reinson, B. A. Zaitlin, R. A. Rahmani, Eds. (Canadian Society of Petroleum Geologists, Mem. 16, 1991), pp. 189–196.
3. D. T. Pugh, *Tides, Surges, and Mean Sea-Level* (Wiley, New York, 1987).
4. The equilibrium tide is defined in terms of an Earth that lacks land masses and has uniform ocean depth and instantaneous tidal propagation speed.
5. M. A. Chan, E. P. Kvale, A. W. Archer, C. P. Sonett, *Geology* **22**, 791 (1994).
6. C. P. Sonett, S. A. Finney, C. R. Williams, *Nature* **335**, 806 (1988); G. E. Williams, *J. Geol. Soc. London* **146**, 97 (1989).
7. T. M. Demko and R. A. Gastaldo, in preparation; T. M. Demko, thesis, University of Alabama (1990).
8. E. P. Kvale, A. W. Archer, H. R. Johnson, *Geology* **17**, 365 (1989); E. P. Kvale and A. W. Archer, in (*2*), pp. 179–188; E. P. Kvale *et al.*, *Geology* **22**, 331 (1994).
9. G. Pannella, in (*10*), pp. 253–284; J. W. Wells, *Nature* **197**, 948 (1963).
10. G. D. Rosenberg and S. K. Runcorn, Eds., *Growth Rhythms and the History of the Earth's Rotation* (Wiley, London, 1975).
11. K. Lambeck, *The Earth's Variable Rotation: Geophysical Causes and Consequences* (Cambridge Univ. Press, Cambridge, 1980).
12. F. D. Stacey, *Physics of the Earth* (Wiley, New York, 1977); W. M. Kaula, *An Introduction to Planetary Physics* (Wiley, New York, 1968).
13. Both the moon and Earth move relative to the center

of mass in such a way as to conserve its position inertially. The present separation of Earth and moon is $3.564 \times 10^{10} \leq 3.84 \times 10^{10} \leq 4.007 \times 10^{10}$ cm [see (18)]. The BCC angular momentum is partitioned between the moon (h_m) and Earth (h_e); Earth has 1.23% of the total system angular momentum, and the moon has the remaining 98.8%. Thus, the moon's present-epoch share of orbital angular momentum must be reduced by 1.23%, the fraction belonging to Earth. For the earlier time periods, the barycenter shifts closer to Earth's center. For the Earth-sun barycenter, the sun is taken as infinitely massive and the moon's mass is ignored. The obliquity of the lunar orbit to Earth's equator is necessarily ignored here.
14. D. S. Broomhead and G. P. King, *Physica D* **20**, 217 (1986); R. P. Vautard, P. Yiou, M. Ghil, *Physica D* **58**, 95 (1992).
15. G. L. Bretthorst, *Bayesian Spectrum Analysis and Parameter Estimation*, Vol. 48 of *Lecture Notes in Statistics*, J. Berger, S. Fienberg, J. Gani, K. Krickeberg, B. Singer, Eds. (Springer-Verlag, Berlin, 1988).
16. In MLE computations, we assume noise is Gaussian (normally distributed). Additionally, as the frequency scale is based on neap-spring laminae count (index) rather than on true frequency, errors attributable to lost laminae can contract the time scale.
17. J. O. Dickey *et al.*, Science **265**, 482 (1994).
18. C. W. Allen, *Astrophysical Quantities* (Althone/Univ. of London Press, London, 1973).
19. G. W. Platzman, *J. Phys. Oceanogr.* **2**, 117 (1972); K. S. Hansen, *Rev. Geophys. Space Phys.* **20**, 457 (1982).
20. W. H. Munk and G. J. F. MacDonald, *The Rotation of the Earth* (Cambridge Univ. Press, Cambridge, 1960).
21. Of the conservation laws for momentum and energy, the former is easiest to deal with because momentum is partitioned primarily between terrestrial rotation and the lunar orbit, whereas energy is partitioned three ways, between these two parameters and frictional loss $f(k_2,Q)$. For constant f, $d\xi/dt$ varies as $\xi^{11/2}$. Conversely, for constant or approximately constant $d\xi/dt$ (Fig. 3), $f \sim \xi^{-11/2}$. Moreover, for constant f, the ratio of k_2 to Q (20) must be constant. It is difficult to assess the invariance of k_2 over the past eon, and perhaps it has changed little, but the tidal lead angle has almost certainly not been fixed—and indeed has probably changed by a large factor—because the terrestrial gravity disturbance field caused by the presence of the moon varies as ξ^{-3}.
22. G. Faure, *Principles of Isotope Geology* (Wiley, New York, 1977); J. S. Kargel and J. S. Lewis, *Icarus* **105**, 1 (1993).
23. H. Takeuchi, *J. Fac. Sci. Univ. Tokyo Sect. 2*, 7 (1951) [quoted in (20)]; *Trans. Am. Geophys. Union* **31**, 651 (1950) [quoted in (10)].
24. In memoriam S. K. Runcorn. Supported in part by the NASA Innovative Research Program (to C.P.S.), the NSF Atmospheres program (to G. E. Williams and C.P.S.) for the Elatina data reduction, and NSF grant EAR-9315937 (to M.A.C. and E.P.K.) for the BCC data. We thank H. R. Johnson and A. Zawostoski for technical support.

19 January 1996; accepted 17 April 1996

T Cell Activation Determined by T Cell Receptor Number and Tunable Thresholds

Antonella Viola and Antonio Lanzavecchia*

The requirements for T cell activation have been reported to vary widely depending on the state of the T cell, the type of antigen-presenting cell, and the nature of the T cell receptor (TCR) ligand. A unitary requirement for T cell responses was revealed by measurement of the number of triggered TCRs. Irrespective of the nature of the triggering ligand, T cells "counted" the number of triggered TCRs and responded when a threshold of ~8000 TCRs was reached. The capacity to reach the activation threshold was severely compromised by a reduction in the number of TCRs. Costimulatory signals lowered the activation threshold to ~1500 TCRs, thus making T cells more sensitive to antigenic stimulation.

T cells are activated when their TCRs are engaged and triggered by ligands on the surface of antigen-presenting cells (APCs). The natural ligand is a complex of a peptide bound to a major histocompatibility complex (MHC) molecule (1), but T cells can also be activated by bacterial superantigens (2) and by antibodies to the TCR-CD3 complex (3). In different experimental systems, the amount of ligand required to activate T cells varies according to the state of the T cells (naïve or memory) and the number of adhesion and costimulatory molecules on the APC (4). A limitation of this type of analysis is that the T cell response can be correlated only to the relative amount of ligand offered, whereas the most relevant parameter—the number of triggered TCRs—remains unknown. This number can now be measured by TCR down-regulation (5). We have used this method to determine the number of triggered TCRs required for the induction of T cell activation and to explain how T cells can respond to very few ligands.

We compared three ligands—complexes of specific peptide and MHC molecules, complexes of the bacterial superantigen TSST (toxic shock syndrome toxin) and MHC molecules, and monovalent antibodies to CD3 (anti-CD3)—with respect to their ability to trigger TCRs and activate T cells (6). All three ligands induced a dose-dependent TCR down-regulation, but the efficiencies and kinetics differed (Fig. 1A).

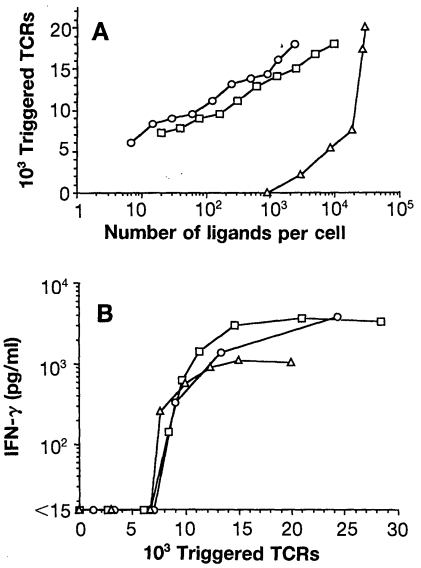

Fig. 1. T cells produce IFN-γ above a threshold of triggered TCRs, regardless of the nature of the stimulus. A $V_\beta 2^+$ T cell clone was stimulated with specific peptide pulsed on autologous EBV-B cells (○), with TSST pulsed on autologous EBV-B cells (□), or with monovalent anti-CD3 in the presence of FcR^+ THP1 cells (△). (**A**) Number of triggered TCRs, measured by TCR down-regulation, as a function of the number of ligands per cell. (**B**) IFN-γ production as a function of the number of triggered TCRs.

As previously shown (5), a small number of peptide-MHC complexes were able to trigger serially a large number of TCRs. Complexes of TSST bound to MHC class II molecules were similarly effective, possibly because TSST-MHC complexes (2), like the peptide-MHC complex (7), bind the TCR with low affinity, thus allowing both triggering and dissociation. Anti-CD3 was much less efficient; the number of TCRs down-regulated was always lower than the number of antibodies offered. The high affinity of binding prevents antibodies from serially triggering TCRs (8).

Although the mode of interaction with TCR-CD3, the kinetics of triggering, and the stoichiometries were different for the three ligands, the responses of the T cells were strikingly similar relative to the number of triggered TCRs. Regardless of the stimulus, T cells produced interferon-γ (IFN-γ) only when ≥ ~8000 TCRs were triggered, and this production rapidly reached a plateau at higher numbers of triggered TCRs (Fig. 1B). The plateau was lower in cells triggered by anti-CD3 (9). The same threshold of activation, both for IFN-γ production and for cell proliferation, was observed with four different $CD4^+$ antigen-specific T cell clones that normally produce IFN-γ in the range of 400 to 20,000 pg/ml. We conclude that T cells "count" the number of triggered TCRs and

Basel Institute for Immunology, Grenzacherstrasse 487, CH 4005 Basel, Switzerland.

*To whom correspondence should be addressed. E-mail: Lanzavecchia@bii.ch